50th AIAA Aerospace Sciences Meeting including the New Horizons Forum and Aerospace Exposition
09 - 12 January 2012, Nashville, Tennessee
AIAA 2012-0138

New Framework for Modeling the Bidirectional Vortex Engine Flowfield with Arbitrary Injection

Georges Akiki* and Joseph Majdalani†
University of Tennessee Space Institute, Tullahoma, TN 37388

In this study, an exact solution is derived for the bidirectional vortex field in a right-cylindrical chamber. The cyclonic motion is assumed to be axisymmetric, steady, inviscid and incompressible, with no accounting for reactions or heat transfer. Our approach is based on the Bragg-Hawthorne equation (BHE), which can be solved in our situation under conditions leading to linearity. Using separation of variables, we are able to identify a set of eigensolutions that may be associated with this problem. The linearity of the resulting BHE enables us to superimpose these eigensolutions while making use of orthogonality to the extent of accommodating different injection configurations that may be imposed at the open boundaries. By way of confirmation, the extended formulation is used to regenerate physical configurations corresponding to five different analytical models found in the literature. The results illustrate how the present idealization may be applied to a variety of incompressible representations of cyclone-driven industrial flow separators, vacuum chambers, furnaces, plasma generators, and liquid rocket engines.

Nomenclature

A_i = inlet area
a = chamber radius
B = tangential angular momentum, ru_θ
b = chamber outlet radius
C = swirl momentum constant
D = tangential surface parameter
H = stagnation pressure head
L = chamber length
l = chamber aspect ratio, L/a
Q_i = inlet volumetric flow rate
r, θ, z = radial, tangential, and axial coordinates
U = mean tangential (inflow) velocity
$U_0(r)$ = arbitrary axial velocity at the headwall
$U_L(r)$ = arbitrary axial velocity at the endwall
u_r = dimensional radial velocity
u_θ = dimensional tangential velocity
u_z = dimensional axial velocity

Symbols

κ = tangential inflow parameter, $(2\pi\sigma l)^{-1}$
λ_n = nth zero of J_1, the Bessel function of the first kind
σ = swirl number
υ = separation constant
ψ = stream function
$\bar{}$ = overbars denote a non-dimensional variable

*Graduate Research Assistant, Mechanical, Aerospace and Biomedical Engineering Department. Member AIAA.
†H. H. Arnold Chair of Excellence in Advanced Propulsion, Mechanical, Aerospace and Biomedical Engineering Department. Associate Fellow AIAA. Fellow ASME.

I. Introduction

BESIDES their emergence in naturally occurring phenomena, cyclonic motions arise in a variety of industrial and propulsion related applications. These swirl-induced patterns are connected to meteorological events such as tornadoes, hurricanes and typhoons, as well as astronomical activities such as cosmic spirals and galactic pinwheels. The bidirectional type of motion is also employed in industrial processes involving cyclonic separators, combustors, and furnaces. Our main interest here is tied to the cyclonic motion that is engendered in the vortex-fired engine class of propulsion devices. This class encompasses several innovative internal combustion devices and thrust chambers such as the Vortex Hybrid Engine introduced by Gloyer, Knuth and Goodman,[1] the Vortex Injection Hybrid Rocket Engine conceived by Knuth *et al*.,[2] the Vortex Combustion Cold-Wall Chamber developed by Chiaverini *et al.*,[3] and the Reverse Vortex Combustor invented by Matveev *et al.*[4]

Given the shortage of purely analytical models of axisymmetric cyclonic flows, an Eulerian-based solution was developed by Vyas, Majdalani and Chiaverini[5-7] using a right-cylindrical Vortex Combustion Cold-Wall Chamber model. Their effort set the pace for a laminar boundary layer treatment of the viscous core. Shortly thereafter, the extension to the hybrid vortex configuration was conceived and carried out by Majdalani and Vyas,[8] and later generalized by Majdalani[9] for the case involving sidewall mass addition. As for the sidewall boundary layers, they were resolved under laminar conditions by Vyas and Majdalani[10] and then, for the axial and radial orientation, by Batterson and Majdalani.[11,12] The latest investigation by Majdalani and Chiaverini[13] formalized the analysis of the tangential boundary layers in a bidirectional vortex, specifically those forming at the core and the sidewall of a swirl-driven cyclonic chamber. A piecewise representation of the problem leading to a Rankine-like vortex was also developed by Maicke and Majdalani.[14] Solutions for other cyclonic flows were obtained by Zhao and Abrahamson[15] who investigated gas cyclones with flow patterns associated with industrial flow separators.

In this paper, we consider the Bragg-Hawthorne equation with assumptions leading to linear source terms. Subsequent analysis based on separation of variables will be employed to uncover three possible types of solutions. After showing that one type is a special case, the remaining two are explored and shown to produce eigensolutions that can be combined linearly. Their superposition leads to a Fourier-like series that, when used in concert with the orthogonality concept to give rise to exact inviscid solutions that can accommodate a specified flow profile at the endwalls. The superposition of these solutions is plausible in our case due to the linearity of the equation being

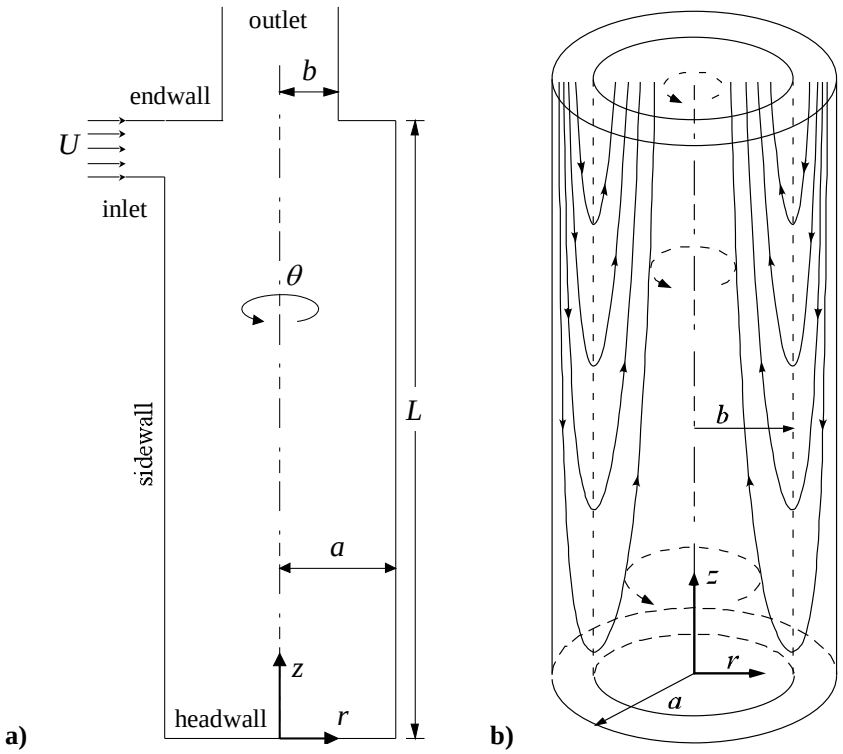

Figure 1. Schematic of the cylindrical bidirectional vortex chamber showing a) geometric and b) flowfield characteristics.

solved. The mathematical framework thus developed enables us to model the flow with realistic inlet and outlet conditions.

II. Formulation

A. Mathematical Model

As we study the axisymmetric bidirectional vortex in a chamber with circular cross-section, cylindrical coordinates are used. Our intent is to solve the applicable equations of motion with the aim of constructing analytical solutions for a user-prescribed set of boundary conditions. Our model is sketched in Fig. 1 where a schematic diagram of the physical problem is provided along with its flowfield characteristics. Note that an inlet section is located near $z = L$ to permit the injection of fluid with arbitrary velocity.

As usual, the incompressible momentum equations for a steady axisymmetric inviscid flow can be written as

$$u_z \frac{\partial u_z}{\partial z} + u_r \frac{\partial u_z}{\partial r} = -\frac{1}{\rho}\frac{\partial p}{\partial z} \tag{1}$$

$$u_z \frac{\partial u_r}{\partial z} + u_r \frac{\partial u_r}{\partial r} - \frac{u_\theta^2}{r} = -\frac{1}{\rho}\frac{\partial p}{\partial r} \tag{2}$$

$$u_z \frac{\partial u_\theta}{\partial z} + u_r \frac{\partial u_\theta}{\partial r} + \frac{u_\theta u_r}{r} = 0 \tag{3}$$

with the attending continuity equation

$$\frac{\partial u_z}{\partial z} + \frac{1}{r}\frac{\partial (r u_r)}{\partial r} = 0 \tag{4}$$

Using the streamfunction ψ, such that $u_z = r^{-1}\partial\psi/\partial r$ and $u_r = -r^{-1}\partial\psi/\partial z$, the above set may be transformed into a single expression known as the Bragg-Hawthorne equation (BHE),

$$\frac{\partial^2\psi}{\partial z^2} + \frac{\partial^2\psi}{\partial r^2} - \frac{1}{r}\frac{\partial\psi}{\partial r} = r^2\frac{\mathrm{d}H}{\mathrm{d}\psi} - B\frac{\mathrm{d}B}{\mathrm{d}\psi} \tag{5}$$

Here $H = p/\rho + \frac{1}{2}u^2$ and $B = ru_\theta$ represent the total pressure head and tangential angular momentum, respectively.

In the absence of friction and heat addition, our model may be taken to be isentropic. This ensures that the total pressure head will remain constant along a streamlines where one may set $\mathrm{d}H/\mathrm{d}\psi = 0$.

To further simplify the problem, we follow the approach used by Majdalani[16] and take the second term on the right-hand-side (RHS) of Eq. (5) to be a linear function of ψ. Thus using C to define the dimensional, *swirl momentum constant*, we put

$$B\frac{\mathrm{d}B}{\mathrm{d}\psi} = C^2\psi \tag{6}$$

and collect

$$\frac{\partial^2\psi}{\partial z^2} + \frac{\partial^2\psi}{\partial r^2} - \frac{1}{r}\frac{\partial\psi}{\partial r} + C^2\psi = 0 \tag{7}$$

Equation (7) can be solved using separation of variables assuming a rigid sidewall with

$$u_r(0,z) = 0 \tag{8}$$

$$u_r(a,z) = 0 \tag{9}$$

Furthermore, arbitrary endwall injection may be accounted for by setting

$$u_z(r,0) = U_0(r) \qquad \text{and} \qquad u_z(r,L) = U_L(r) \tag{10}$$

where $U_0(r)$ and $U_L(r)$ can be user-specified to capture realistic flow patterns that observe the mass conservation principle. Substituting $\psi(z,r) = Z(z)R(r)$ into Eq. (7) leads to

$$-\frac{1}{Z(z)}\frac{\mathrm{d}^2Z(z)}{\mathrm{d}z^2} = \frac{1}{R(r)}\frac{\mathrm{d}^2R(r)}{\mathrm{d}r^2} - \frac{1}{rR(r)}\frac{\mathrm{d}R(r)}{\mathrm{d}r} + C^2 = \begin{cases} 0 \\ \pm\upsilon^2 \end{cases} \tag{11}$$

Clearly, three cases may be identified and promptly classified as

Type 0 with $\mathrm{RHS} = 0$:

$$\psi(r,z) = r\left(C_1 z + C_2\right)\left[C_3 J_1(Cr) + C_4 Y_1(Cr)\right] \tag{12}$$

Type I with $\mathrm{RHS} = +\upsilon^2$:

$$\psi(r,z) = r\left[C_1 \sin(\upsilon\, z) + C_2 \cos(\upsilon\, z)\right]\left[C_3 J_1\left(r\sqrt{C^2-\upsilon^2}\right) + C_4 Y_1\left(r\sqrt{C^2-\upsilon^2}\right)\right] \tag{13}$$

Type II with $\text{RHS} = -\upsilon^2$:

$$\psi(r,z) = r\left[C_1 \sinh(\upsilon\, z) + C_2 \cosh(\upsilon\, z)\right]\left[C_3 J_1\left(r\sqrt{C^2+\upsilon^2}\right) + C_4 Y_1\left(r\sqrt{C^2+\upsilon^2}\right)\right] \tag{14}$$

When imposing the centerline condition defined by Eq. (8), it may be realized that $C_4 = 0$ will eliminate the singularity for $r \to 0$ in $Y_1(Cr)$, $Y_1[r(C^2-\upsilon^2)^{\frac{1}{2}}]$ and $Y_1[r(C^2+\upsilon^2)^{\frac{1}{2}}]$. The solution set reduces to

$$\psi(r,z) = \begin{cases} r\left(K_1 z + K_2\right) J_1(Cr) & \text{(type 0)} \\ r\left[K_1 \sin(\upsilon\, z) + K_2 \cos(\upsilon\, z)\right] J_1\left(r\sqrt{C^2-\upsilon^2}\right) & \text{(type I)} \\ r\left[K_1 \sinh(\upsilon\, z) + K_2 \cosh(\upsilon\, z)\right] J_1\left(r\sqrt{C^2+\upsilon^2}\right) & \text{(type II)} \end{cases} \tag{15}$$

where $K_1 = C_1 C_3$ and $K_2 = C_2 C_3$. At this point one may apply Eq. (9), the rigid wall requirement on the radial velocity, to extract two sets of eigenvalues:

$$J_1\left(a\sqrt{C^2-\upsilon^2}\right) = 0 \qquad \text{or} \qquad \upsilon = \upsilon_n = \sqrt{C^2 - \lambda_n^2/a^2} \qquad \text{(type I)} \tag{16}$$

$$J_1\left(a\sqrt{C^2+\upsilon^2}\right) = 0 \qquad \text{or} \qquad \upsilon = \upsilon_n^* = \sqrt{\lambda_n^2/a^2 - C^2} \qquad \text{(type II)} \tag{17}$$

where $\lambda_n = (3.83171, 7.01559, 10.1735, 13.3237, \ldots)$ designates the set of roots connected with the Bessel function of the first kind. In what follows, the multivalued nature of λ_n warrants the use of both expressions for υ_n and υ_n^*. In the type 0 formulation, the streamfunction remains independent of υ, a situation that leads to a less general solution, in which C remains single-valued, as prescribed by Eq. (6). A more comprehensive framework may be achieved by summing over all λ_n and putting, for the type I and type II solutions,

$$\psi(r,z) = \begin{cases} \displaystyle\sum_{n=0}^{\infty} r\left[K_{1n} \sin(\upsilon_n z) + K_{2n} \cos(\upsilon_n z)\right] J_1(\lambda_n r/a) & \text{(type I)} \\ \displaystyle\sum_{n=0}^{\infty} r\left[K_{1n} \sinh(\upsilon_n^* z) + K_{2n} \cosh(\upsilon_n^* z)\right] J_1(\lambda_n r/a) & \text{(type II)} \end{cases} \tag{18}$$

and, for the corresponding axial velocity,

$$u_z = \begin{cases} \displaystyle\sum_{n=0}^{\infty}\left[K_{1n} \sin(\upsilon_n z) + K_{2n} \cos(\upsilon_n z)\right] \frac{\lambda_n}{a} J_0\left(\frac{\lambda_n}{a} r\right) & \text{(type I)} \\ \displaystyle\sum_{n=0}^{\infty}\left[K_{1n} \sinh(\upsilon_n^* z) + K_{2n} \cosh(\upsilon_n^* z)\right] \frac{\lambda_n}{a} J_0\left(\frac{\lambda_n}{a} r\right) & \text{(type II)} \end{cases} \tag{19}$$

At this junction, an arbitrary velocity profile may be imposed at the endwalls by specifying $u_z(r,0) = U_0(r)$ and $u_z(r,L) = U_L(r)$ as per Eq. (10). Using the orthogonality function, we recall that

$$\int_0^a r J_0(mr) J_0(nr)\,\mathrm{d}r = \begin{cases} 0; & m \neq n \\ \frac{1}{2} a^2 J_0^2(ma); & m = n \end{cases} \tag{20}$$

Then through backward substitutions, the two constants K_{1n} and K_{2n} may be extracted and written as

$$K_{1n} = \begin{cases} \dfrac{I_L - \cos(\upsilon_n L) I_0}{\lambda_n a J_0^2(\lambda_n) \sin(\upsilon_n L)} \\ \dfrac{I_L - \cosh(\upsilon_n^* L) I_0}{\lambda_n a J_0^2(\lambda_n) \sinh(\upsilon_n^* L)} \end{cases} \quad \text{and} \quad K_{2n} = \begin{cases} \dfrac{I_0}{\lambda_n a J_0^2(\lambda_n)} \\ \dfrac{I_0}{\lambda_n a J_0^2(\lambda_n)} \end{cases} \tag{21}$$

In the above, the source terms may be determined from

$$I_0 \equiv 2\int_0^a U_0(r) r J_0(\lambda_n r/a)\,\mathrm{d}r \quad \text{and} \quad I_L \equiv 2\int_0^a U_L(r) r J_0(\lambda_n r/a)\,\mathrm{d}r \tag{22}$$

Inserting these relations back into Eq. (18) and differentiating, general expressions for the axial and radial velocities may be returned. These are

$$u_z = \begin{cases} \displaystyle\sum_{n=0}^{\infty}\left[\frac{I_L-\cos(\upsilon_n L)I_0}{\lambda_n a J_0^2(\lambda_n)}\frac{\sin(\upsilon_n z)}{\sin(\upsilon_n L)}+\frac{I_0}{\lambda_n a J_0^2(\lambda_n)}\cos(\upsilon_n z)\right]\frac{\lambda_n}{a}J_0\left(\frac{\lambda_n}{a}r\right) & \text{(type I)} \\ \displaystyle\sum_{n=0}^{\infty}\left[\frac{I_L-\cosh(\upsilon_n^* L)I_0}{\lambda_n a J_0^2(\lambda_n)}\frac{\sinh(\upsilon_n^* z)}{\sinh(\upsilon_n^* L)}+\frac{I_0}{\lambda_n a J_0^2(\lambda_n)}\cosh(\upsilon_n^* z)\right]\frac{\lambda_n}{a}J_0\left(\frac{\lambda_n}{a}r\right) & \text{(type II)} \end{cases} \tag{23}$$

and

$$u_r = \begin{cases} -\displaystyle\sum_{n=0}^{\infty}\left[\frac{I_L-\cos(\upsilon_n L)I_0}{\lambda_n a J_0^2(\lambda_n)}\frac{\upsilon_n}{\sin(\upsilon_n L)}\cos(\upsilon_n z)-\frac{I_0}{\lambda_n a J_0^2(\lambda_n)}\upsilon_n\sin(\upsilon_n z)\right]J_1\left(\frac{\lambda_n}{a}r\right) & \text{(type I)} \\ -\displaystyle\sum_{n=0}^{\infty}\left[\frac{I_L-\cosh(\upsilon_n^* L)I_0}{\lambda_n a J_0^2(\lambda_n)}\frac{\upsilon_n^*}{\sinh(\upsilon_n^* L)}\cosh(\upsilon_n^* z)+\frac{I_0}{\lambda_n a J_0^2(\lambda_n)}\upsilon_n^*\sinh(\upsilon_n^* z)\right]J_1\left(\frac{\lambda_n}{a}r\right) & \text{(type II)} \end{cases} \tag{24}$$

As for the tangential velocity u_θ, we can start with Eq. (6) and integrate $\int B\mathrm{d}B = \int C_n^2\psi\mathrm{d}\psi$ to obtain

$$B^2 = C^2\psi^2 + D \quad \text{or} \quad u_\theta = r^{-1}\sqrt{C^2\psi^2+D} \tag{25}$$

where D may be dubbed the tangential surface parameter as it can be specified by the wall boundary condition imposed on u_θ. Then by inserting ψ into Eq. (25), an expanded form of u_θ may be arrived at, specifically

$$ru_\theta = \begin{cases} \left\{C^2\left[\displaystyle\sum_{n=0}^{\infty} r\left(\frac{I_L-\cos(\upsilon_n L)I_0}{\lambda_n a J_0^2(\lambda_n)}\frac{\sin(\upsilon_n z)}{\sin(\upsilon_n L)}+\frac{I_0}{\lambda_n a J_0^2(\lambda_n)}\cos(\upsilon_n z)\right)J_1\left(\frac{\lambda_n}{a}r\right)\right]^2+D\right\}^{\frac{1}{2}} & \text{(type I)} \\ \left\{C^2\left(\displaystyle\sum_{n=0}^{\infty} r\left[\frac{I_L-\cosh(\upsilon_n^* L)I_0}{\lambda_n a J_0^2(\lambda_n)}\frac{\sinh(\upsilon_n^* z)}{\sinh(\upsilon_n^* L)}+\frac{I_0}{\lambda_n a J_0^2(\lambda_n)}\cosh(\upsilon_n^* z)\right]J_1\left(\frac{\lambda_n}{a}r\right)\right)^2+D\right\}^{\frac{1}{2}} & \text{(type II)} \end{cases} \tag{26}$$

Note that C appears outside the summation due to nonlinearity in the relation between u_θ and ψ. It therefore retains a unique value irrespective of the eigensolutions that are being superimposed in the angular momentum expression given by Eq. (26).

B. Consolidated Solution

At first glance, the two types of solutions captured in Eqs. (23), (24), and (26) appear dissimilar. Upon further scrutiny, however, we find that one may be restored from the other for $\upsilon_n^2 = i^2(\upsilon_n^*)^2$ or $\upsilon_n = \pm i(\upsilon_n^*)$. This is due to the trigonometric identities

$$\begin{cases} \cosh x = \cos(ix) \\ \sinh x = -i\sin(ix) \end{cases} \quad \text{or} \quad \begin{cases} \cosh\upsilon_n^* = \cos(i\upsilon_n^*) = \cos\upsilon_n \\ \sinh\upsilon_n^* = -i\sin(i\upsilon_n^*) = -i\sin(\pm ii\upsilon_n) = \pm i\sin(\upsilon_n) \end{cases} \tag{27}$$

These are needed to switch from type II to type I representation, or conversely, through

$$\begin{cases} \cos x = \cosh(ix) \\ \sin x = -i\sinh(ix) \end{cases} \quad \text{or} \quad \begin{cases} \cos\upsilon_n = \cosh(i\upsilon_n) = \cosh(\upsilon_n^*) \\ \sin\upsilon_n = -i\sinh(i\upsilon_n) = -i\sinh(\pm ii\upsilon_n^*) = \pm i\sinh(\upsilon_n^*) \end{cases} \tag{28}$$

These identities enable us to confirm by inspection the equality of the two types of solutions obtained for u_θ and u_z. In the interest of clarity, we show how this can be performed for u_r. By substituting $\upsilon_n^* = \pm i\upsilon_n$ into the second member of Eq. (24) and using both $\cosh(i\upsilon_n z) = \cos(\upsilon_n z)$ and $\sinh(i\upsilon_n z) = i\sin(\upsilon_n z)$, we have

$$\begin{aligned} u_r &= -\sum_{n=0}^{\infty}\left[\frac{I_L-\cosh(\pm i\upsilon_n L)I_0}{\lambda_n a J_0^2(\lambda_n)}\frac{(\pm i\upsilon_n)}{\sinh(\pm i\upsilon_n L)}\cosh(\pm i\upsilon_n z)+\frac{I_0}{\lambda_n a J_0^2(\lambda_n)}(\pm i\upsilon_n)\sinh(\pm i\upsilon_n z)\right]J_1\left(\frac{\lambda_n}{a}r\right) \\ &= -\sum_{n=0}^{\infty}\left[\frac{I_L-\cos(\upsilon_n L)I_0}{\lambda_n a J_0^2(\lambda_n)}\frac{i\upsilon_n}{i\sin(\upsilon_n L)}\cos(\upsilon_n z)+\frac{I_0}{\lambda_n a J_0^2(\lambda_n)}(i\upsilon_n)i\sin(\upsilon_n z)\right]J_1\left(\frac{\lambda_n}{a}r\right) \end{aligned} \tag{29}$$

The outcome is of course identical to the type I representation.

Given that λ_n can vary from 3.8317 to ∞ while C remains fixed, the sign of $C^2 - \lambda_n^2/a^2$ can be either positive or negative. Then using the subscript indicial k to denote the largest Bessel root to satisfy $\lambda_k \le aC$, one may identify two subsets that exhibit the following properties

$$\begin{cases} \upsilon_n^2 = C^2 - \lambda_n^2 / a^2 \geq 0; \quad \lambda_n \leq aC; \quad n = 0,\ldots,k \\ (\upsilon_n^*)^2 = \lambda_n^2 / a^2 - C^2 > 0; \quad \lambda_n > aC; \quad n = k+1,\ldots,\infty \end{cases} \tag{30}$$

In each of these subsets, υ_n and υ_n^* remain essentially positive real numbers. Then owing to the identity of the type I and type II expressions, a consolidated formulation may be constructed with no imaginary parts. This is accomplished by taking

$$\begin{aligned} \psi(r,z) = \sum_{n=0}^{k} r\left[\frac{I_L - \cos(\upsilon_n L) I_0}{\lambda_n a J_0^2(\lambda_n)\sin(\upsilon_n L)}\sin(\upsilon_n z) + \frac{I_0}{\lambda_n a J_0^2(\lambda_n)}\cos(\upsilon_n z)\right] J_1\left(\frac{\lambda_n}{a} r\right) \\ + \sum_{n=k+1}^{\infty} r\left[\frac{I_L - \cosh(\upsilon_n^* L) I_0}{\lambda_n a J_0^2(\lambda_n)\sinh(\upsilon_n^* L)}\sinh(\upsilon_n^* z) + \frac{I_0}{\lambda_n a J_0^2(\lambda_n)}\cosh(\upsilon_n^* z)\right] J_1\left(\frac{\lambda_n}{a} r\right) \end{aligned} \tag{31}$$

Similarly, u_z, u_r and u_θ may be expressed as:

$$u_z = \left\{ \begin{aligned} &\sum_{n=0}^{k}\left[\frac{I_L - \cos(\upsilon_n L) I_0}{\lambda_n a J_0^2(\lambda_n)\sin(\upsilon_n L)}\sin(\upsilon_n z) + \frac{I_0}{\lambda_n a J_0^2(\lambda_n)}\cos(\upsilon_n z)\right]\frac{\lambda_n}{a} J_0\left(\frac{\lambda_n}{a} r\right) \\ &+ \sum_{n=k+1}^{\infty}\left[\frac{I_L - \cosh(\upsilon_n^* L) I_0}{\lambda_n a J_0^2(\lambda_n)\sinh(\upsilon_n^* L)}\sinh(\upsilon_n^* z) + \frac{I_0}{\lambda_n a J_0^2(\lambda_n)}\cosh(\upsilon_n^* z)\right]\frac{\lambda_n}{a} J_0\left(\frac{\lambda_n}{a} r\right) \end{aligned} \right\} \tag{32}$$

$$u_r = \left\{ \begin{aligned} &-\sum_{n=0}^{k}\left[\frac{I_L - \cos(\upsilon_n L) I_0}{\lambda_n a J_0^2(\lambda_n)\sin(\upsilon_n L)}\upsilon_n \cos(\upsilon_n z) - \frac{I_0}{\lambda_n a J_0^2(\lambda_n)}\upsilon_n \sin(\upsilon_n z)\right] J_1\left(\frac{\lambda_n}{a} r\right) \\ &- \sum_{n=k+1}^{\infty}\left[\frac{I_L - \cosh(\upsilon_n^* L) I_0}{\lambda_n a J_0^2(\lambda_n)\sinh(\upsilon_n^* L)}\upsilon_n^* \cosh(\upsilon_n^* z) + \frac{I_0}{\lambda_n a J_0^2(\lambda_n)}\upsilon_n^* \sinh(\upsilon_n^* z)\right] J_1\left(\frac{\lambda_n}{a} r\right) \end{aligned} \right\} \tag{33}$$

and

$$u_\theta = \left(C^2 \left\{ \begin{aligned} &\sum_{n=0}^{k}\left[\frac{I_L - \cos(\upsilon_n L) I_0}{\lambda_n a J_0^2(\lambda_n)\sin(\upsilon_n L)}\sin(\upsilon_n z) + \frac{I_0}{\lambda_n a J_0^2(\lambda_n)}\cos(\upsilon_n z)\right] J_1\left(\frac{\lambda_n}{a} r\right) \\ &+ \sum_{n=k+1}^{\infty}\left[\frac{I_L - \cosh(\upsilon_n^* L) I_0}{\lambda_n a J_0^2(\lambda_n)\sinh(\upsilon_n^* L)}\sinh(\upsilon_n^* z) + \frac{I_0}{\lambda_n a J_0^2(\lambda_n)}\cosh(\upsilon_n^* z)\right] J_1\left(\frac{\lambda_n}{a} r\right) \end{aligned} \right\}^2 + \frac{D}{r^2} \right)^{\frac{1}{2}} \tag{34}$$

Equations (32), (33) and (34) constitute the apex of this study and are, therefore, marked as such. To employ this formulation, the arbitrary axial profiles $U_L(r)$ and $U_0(r)$ may be defined based on realistic flow conditions. The specification of u_z at the endwalls leads to the full determination of the source integrals (I_0, I_l). These affect the expression for u_θ. Nonetheless, two additional parameters remain available to control u_θ and enable us to mimic a realistic tangential velocity at entry. The tangential velocity may be hence prescribed by specifying the constants C and D in a manner to match a given injection function at the endwall. For example, when $D = 0$, a special family of Trkalian flows may be engendered in which no slippage is permitted at the sidewall. Conversely, when $D \neq 0$, an essential singularity ascribed to swirl-dominated inviscid flows appears at the centerline. Once C, I_0 and I_l are determined, both u_z and u_r become known throughout the entire domain. Evidently, any velocity pattern imposed at $z = (0, L)$ will have to satisfy volume conservation viz.

$$\int_0^a 2\pi r\left[u_z(r,L) - u_z(r,0)\right]\mathrm{d}r = 0 \tag{35}$$

C. Normalization

Using standard reference values, one may introduce

$$\bar{r}=\frac{r}{a},\ \bar{z}=\frac{z}{a},\ \bar{u}_r=\frac{u_r}{U},\ \bar{u}_z=\frac{u_z}{U},\ \bar{u}_\theta=\frac{u_\theta}{U},\ \bar{\psi}=\frac{\psi}{Ua^2},\ \bar{Q}_i=\frac{Q_i}{Ua^2},\ \bar{D}=\frac{D}{U^2a^2},\ \bar{C}=Ca \tag{36}$$

where $\bar{D}$ and $\bar{C}$ represent the non-dimensional forms of the tangential surface parameter and swirl momentum constant, respectively. Implementing the above normalization into our equations, the streamfunction and velocity expressions become

$$\begin{aligned}\bar{\psi}(\bar{r},\bar{z})=&\sum_{n=0}^{k}\bar{r}\left[\frac{\bar{I}_L-\cos(\bar{\upsilon}_n l)\bar{I}_0}{\lambda_n J_0^2(\lambda_n)\sin(\bar{\upsilon}_n l)}\sin(\bar{\upsilon}_n\bar{z})+\frac{\bar{I}_0}{\lambda_n J_0^2(\lambda_n)}\cos(\bar{\upsilon}_n\bar{z})\right]J_1(\lambda_n\bar{r})\\&+\sum_{n=k+1}^{\infty}r\left[\frac{\bar{I}_L-\cosh(\bar{\upsilon}_n^* l)\bar{I}_0}{\lambda_n J_0^2(\lambda_n)\sinh(\bar{\upsilon}_n^* l)}\sinh(\bar{\upsilon}_n^*\bar{z})+\frac{\bar{I}_0}{\lambda_n J_0^2(\lambda_n)}\cosh(\bar{\upsilon}_n^*\bar{z})\right]J_1(\lambda_n\bar{r})\end{aligned} \tag{37}$$

$$\begin{aligned}\bar{u}_z(\bar{r},\bar{z})=&\sum_{n=0}^{k}\left[\frac{\bar{I}_l-\cos(\bar{\upsilon}_n l)\bar{I}_0}{\lambda_n J_0^2(\lambda_n)\sin(\bar{\upsilon}_n l)}\sin(\bar{\upsilon}_n\bar{z})+\frac{\bar{I}_0}{\lambda_n J_0^2(\lambda_n)}\cos(\bar{\upsilon}_n\bar{z})\right]\lambda_n J_0(\lambda_n\bar{r})\\&+\sum_{n=k+1}^{\infty}\left[\frac{\bar{I}_l-\cosh(\bar{\upsilon}_n^* l)\bar{I}_0}{\lambda_n J_0^2(\lambda_n)\sinh(\bar{\upsilon}_n^* l)}\sinh(\bar{\upsilon}_n^*\bar{z})+\frac{\bar{I}_0}{\lambda_n J_0^2(\lambda_n)}\cosh(\bar{\upsilon}_n^*\bar{z})\right]\lambda_n J_0(\lambda_n\bar{r})\end{aligned} \tag{38}$$

$$\begin{aligned}\bar{u}_r(\bar{r},\bar{z})=&-\sum_{n=0}^{k}\left[\frac{\bar{I}_l-\cos(\bar{\upsilon}_n l)\bar{I}_0}{\lambda_n J_0^2(\lambda_n)\sin(\bar{\upsilon}_n l)}\bar{\upsilon}_n\cos(\bar{\upsilon}_n\bar{z})-\frac{\bar{I}_0}{\lambda_n J_0^2(\lambda_n)}\bar{\upsilon}_n\sin(\bar{\upsilon}_n\bar{z})\right]J_1(\lambda_n\bar{r})\\&-\sum_{n=k+1}^{\infty}\left[\frac{\bar{I}_l-\cosh(\bar{\upsilon}_n^* l)\bar{I}_0}{\lambda_n J_0^2(\lambda_n)\sinh(\bar{\upsilon}_n^* l)}\bar{\upsilon}_n^*\cosh(\bar{\upsilon}_n\bar{z})+\frac{\bar{I}_0}{\lambda_n J_0^2(\lambda_n)}\bar{\upsilon}_n^*\sinh(\bar{\upsilon}_n^*\bar{z})\right]J_1(\lambda_n\bar{r})\end{aligned} \tag{39}$$

and, for the tangential component,

$$\begin{aligned}\bar{u}_\theta(\bar{r},\bar{z})=&\left(\bar{C}^2\left\{\sum_{n=0}^{k}\left[\frac{\bar{I}_l-\cos(\bar{\upsilon}_n l)\bar{I}_0}{\lambda_n a J_0^2(\lambda_n)\sin(\bar{\upsilon}_n l)}\sin(\bar{\upsilon}_n\bar{z})+\frac{\bar{I}_0}{\lambda_n a J_0^2(\lambda_n)}\cos(\bar{\upsilon}_n\bar{z})\right]J_1(\lambda_n\bar{r})\right.\right.\\&\left.\left.+\sum_{n=k+1}^{\infty}\left[\frac{\bar{I}_l-\cosh(\bar{\upsilon}_n^* l)\bar{I}_0}{\lambda_n J_0^2(\lambda_n)\sinh(\bar{\upsilon}_n^* l)}\sinh(\bar{\upsilon}_n^*\bar{z})+\frac{\bar{I}_0}{\lambda_n J_0^2(\lambda_n)}\cosh(\bar{\upsilon}_n^*\bar{z})\right]J_1(\lambda_n\bar{r})\right\}^2+\frac{\bar{D}}{\bar{r}^2}\right)^{\frac{1}{2}}\end{aligned} \tag{40}$$

Here the normalized source integrals may be computed from

$$\begin{cases}\bar{I}_l\equiv 2\int_0^1\bar{u}_z(\bar{r},l)\bar{r}J_0(\lambda_n\bar{r})\,\mathrm{d}\bar{r} & \text{(endwall)}\\ \bar{I}_0\equiv 2\int_0^1\bar{u}_z(\bar{r},0)\bar{r}J_0(\lambda_n\bar{r})\,\mathrm{d}\bar{r} & \text{(headwall)}\end{cases} \tag{41}$$

where $\bar{\upsilon}_n^2=\bar{C}^2-\lambda_n^2$ and $(\bar{\upsilon}_n^*)^2=\lambda_n^2-\bar{C}^2$. It may be instructive to note that the foregoing solution can accommodate arbitrary headwall and endwall velocity patterns, $\bar{u}_z(\bar{r},0)$ and $\bar{u}_z(\bar{r},l)$, so long as the imposed profiles remain observant of the mass conservation principle. Otherwise, the solution initiated with an incongruent model will be self-corrected in the resulting series representation that produces a distribution which, when evaluated at the endwalls, will generate a velocity profile that is different from the one originally imposed. The altered profile at the boundary will strongly resemble the one prescribed as an input except for some minor differences that cause it to gracefully satisfy mass conservation. Conversely, when a physical solution that observes continuity is imposed at the endwalls, the resulting series summation will return the same profile as the input source. Such self-correcting behavior is quite interesting to note in the present model. It may be ascribed to the series solution being analytic, continuous and infinitely differentiable, in addition to being consistent with mass conservation throughout the entire chamber. These properties instill in our solution an aversion towards unphysical jumps, especially at its boundaries.

III. Results and Discussion

Several analytical models for the cold bidirectional vortex engine can be found in the literature. The most prominent of these are listed in Table 1. Note that none of these models incorporate fuel injection at the headwall. In order to

Table 1. Various analytical models for the bidirectional vortex in a confined cylindrical chamber

Model	Velocity Profile
Beltramian model ($\upsilon = 0$)	$-c\kappa J_1(\lambda_0 \bar{r})\mathbf{e}_r + c\lambda_0 \kappa \bar{z} J_1(\lambda_0 \bar{r})\mathbf{e}_\theta + c\lambda_0 \kappa \bar{z} J_0(\lambda_0 \bar{r})\mathbf{e}_z$
Trkalian model ($\upsilon = 0$)	$-c\kappa J_1(\lambda_0 \bar{r})\mathbf{e}_r + \frac{1}{\bar{r}}\sqrt{1 + c^2\lambda_0^2\kappa^2\bar{r}^2\bar{z}^2 J_1^2(\lambda_0 \bar{r})}\mathbf{e}_\theta + c\lambda_0 \kappa \bar{z} J_0(\lambda_0 \bar{r})\mathbf{e}_z$
Beltramian model ($\upsilon = \frac{1}{2}\pi / L$)	$-\frac{1}{2}\pi c\kappa \cos(\frac{1}{2}\pi \bar{z} / l) J_1(\lambda_0 \bar{r})\mathbf{e}_r + c\lambda_0 \kappa l \sin(\frac{1}{2}\pi \bar{z} / l) J_0(\lambda_0 \bar{r})\mathbf{e}_z$ $+\frac{1}{2}\pi c\kappa \sqrt{1 + 4\lambda_0^2 l^2 / \pi^2}\, \sin(\frac{1}{2}\pi \bar{z} / l) J_1(\lambda_0 \bar{r})\mathbf{e}_\theta$
Trkalian model ($\upsilon = \frac{1}{2}\pi / L$)	$-\frac{1}{2}\pi c\kappa \cos(\frac{1}{2}\pi \bar{z} / l) J_1(\lambda_0 \bar{r})\mathbf{e}_r + c\lambda_0 \kappa l \sin(\frac{1}{2}\pi \bar{z} / l) J_0(\lambda_0 \bar{r})\mathbf{e}_z$ $+\frac{1}{\bar{r}}\sqrt{1 + c^2\kappa^2(\lambda_0^2 l^2 + \frac{1}{4}\pi^2)\bar{r}^2 J_1^2(\lambda_0 \bar{r}) \sin^2(\frac{1}{2}\pi \bar{z} / l)}\mathbf{e}_\theta$
Complex-Lamellar model	$-\frac{\sin(\pi \bar{r}^2)}{2\pi\sigma l \sin(\pi\beta^2)}\mathbf{e}_r + \frac{1}{\bar{r}}\mathbf{e}_\theta + \frac{\bar{z}\cos(\pi \bar{r}^2)}{\sigma l \sin(\pi\beta^2)}\mathbf{e}_z$

mimic the no-fuel injection scenario in our model, the headwall velocity $U_0(r)$ will be set to zero. Conversely, the endwall velocity $U_L(r)$ will be set equal to the axial profile at the inlet boundary of the model to be examined.

A. Axial Velocity

Our procedure consists of using the boundary conditions at the endwalls to fix the inlet and outlet axial velocities, before selecting the independent parameters, $\bar{C}$ and $\bar{D}$, in such a way to reproduce, as closely as possible, the desired tangential velocity at $\bar{z} = l$. The resulting formulation can then be employed to evaluate the axial velocity over the entire chamber domain, including the endwall boundaries, where a verification of the input profile imposed initially may be undertaken. To illustrate this process, the Beltramian and Trkalian profiles posted in Table 1 are chosen as benchmarks. Using their endwall values at $\bar{z} = l$ as inflow requirements in Eq. (38), the ensuing description for $\bar{u}_z$ may be readily obtained. Corresponding results are displayed in Fig. 2a for $\upsilon = 0$ and Fig. 3a for $\upsilon = \pi / 2L$, at several axial stations extending from the headwall to the endwall. The axial solutions produced directly from Majdalani[16] without series summations are shown on the right-hand-side parts (b) of the same graphs. These happen to be identical for the Beltramian and Trkalian configurations obtained for each of $\upsilon = 0$ (Fig. 2b) and $\upsilon = \pi / 2L$ (Fig. 3b), respectively. It can be seen that the present model regenerates the same outcome as before in both flow configurations. The striking resemblance observed in these illustrations may be attributed to the two analyses being based on analogous approximations and assumptions at their points of departure, including their reliance on a linear BHE and a consistent set of physical requirements. Furthermore, the eigenvalue

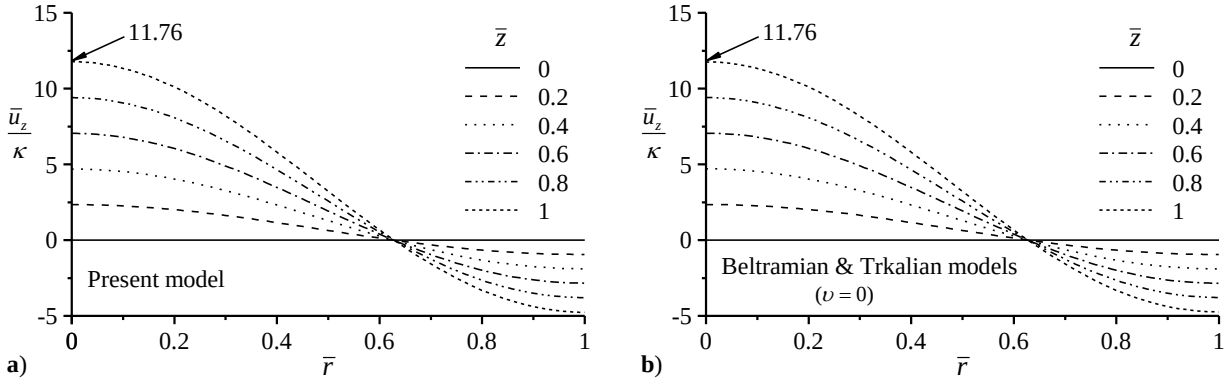

Figure 2. Comparison between axial velocities corresponding to a) Eq. (38) and b) the linear Beltramian and Trkalian formulations obtained by Majdalani[16] with $\upsilon = 0$. Here $l = 1$.

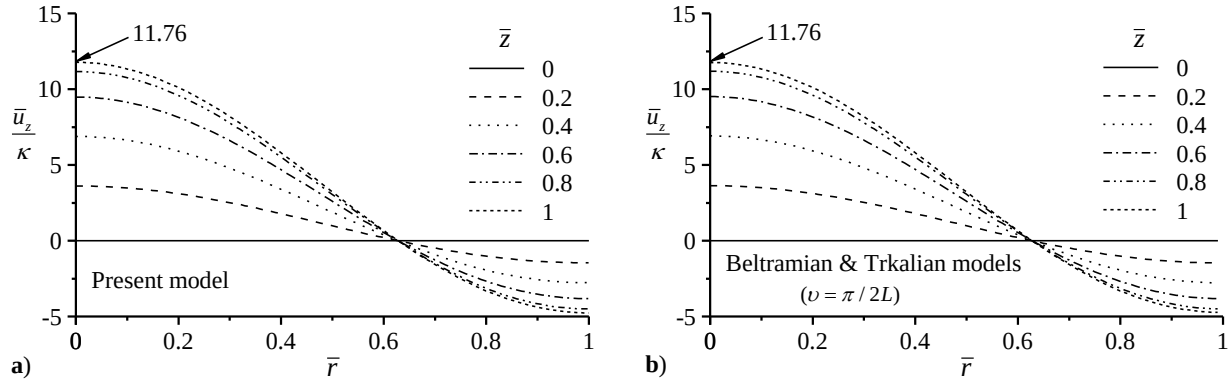

Figure 3. Comparison between axial velocities corresponding to a) Eq. (38) and b) the linear Beltramian and Trkalian formulations obtained by Majdalani[16] with $\upsilon = \pi/(2L)$. Here l = 1.

λ_0 used by Majdalani[16] in defining the aforementioned cases belongs to the subset of eigenvalues that are built into the generalized framework developed here.

To further visualize the behavior of Eq. (38), $\bar{u}_z$ is presented in Fig. 4 where it is compared to the complex-lamellar counterpart constructed by Vyas and Majdalani.[17] Unlike the Vyas-Majdalani motion in which the axial velocity along the centerline (or sidewall) increases (or decreases) linearly with the distance from the headwall, the acceleration associated with the present model is spatially variant. As it may be inferred from Fig. 4a, the axial variation of $\bar{u}_z$ follows a nonlinear trend, in contrast to the linear behavior of the complex-lamellar solution. This may be attributed to the latter originating from a different BHE formulation than the one utilized here.

Returning to Fig. 4b, a fixed locus of the mantle may be seen at $\bar{r} = 0.707$, a key characteristic of the complex-lamellar model, irrespective of the axial position. Conversely, the location of the series approximation in Fig. 4a is seen to slightly shift along the axis of the chamber, starting from $\bar{r} = 0.707$ at $\bar{z} = l$, where the simulated profile is imposed, to a value approaching 0.63 that is characteristic of both Beltramian and Trkalian solutions.

B. Tangential Velocity

The tangential velocity at $\bar{z} = l$ is dependent on the choice of $\bar{u}_z(\bar{r}, l)$. The two constants C and D lend us two degrees of freedom by providing two parameters that can be adjusted to the extent of accounting for different tangential velocity profiles at the endwalls. To demonstrate the flexibility of our solution, we consider the Beltramian and Trkalian axial profiles by Majdalani[16] for $\upsilon = \pi / 2L$, where each model features a different tangential velocity at the inlet.

Figure 5a is based on Eq. (40) using Majdalani's slip-resistant Trkalian profile in the axial direction.[16] In this case, we set $\bar{D} = 0$ in the tangential velocity expression in order to ensure that it vanishes at $\bar{r} = 0$. We then adjust the parameter $\bar{C}$ to match the magnitude of the velocity at the endwall. Because the inlet tangential speed observes the no-slip requirement at the sidewall, the velocity-adherence property is maintained along the entire length of the wall. For example, it can be seen that $\bar{u}_\theta$ at $\bar{r} = 1$ vanishes for $0 \le \bar{z} \le l$. Evidently such will not be the behavior

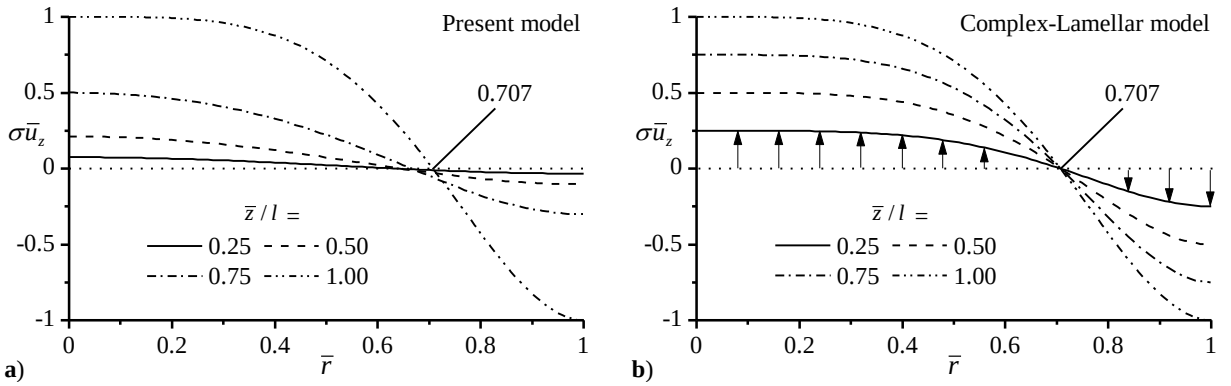

Figure 4. Comparison between the axial velocities corresponding to a) Eq. (38) and b) the complex-lamellar solution.

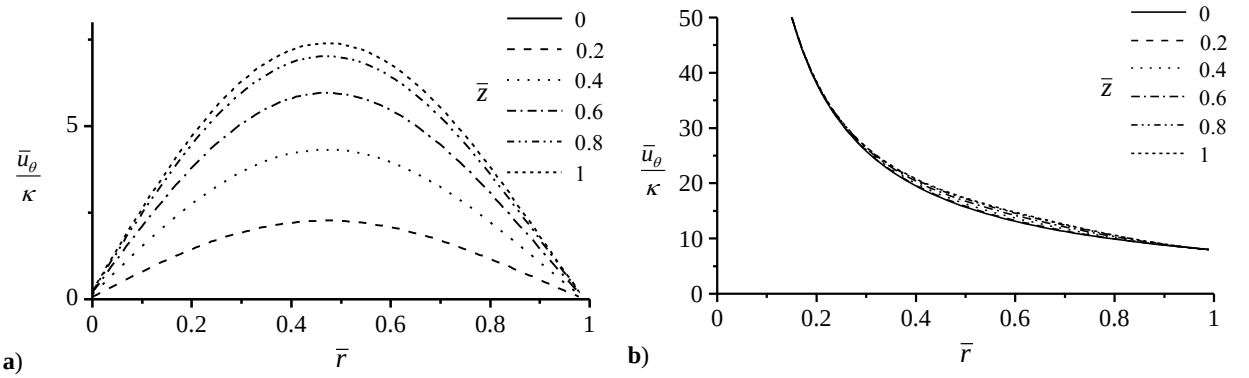

Figure 5. Radial distribution of the tangential velocity at different axial positions for a) Trkalian and b) Beltramian input conditions. Here l = 1 and κ= 0.125.

under different inlet conditions, especially when using motions that permit slip at the sidewall.

Our second test case provides an illustration of the latter situation. Now we use the linearly varying Beltramian profile with a slip permitting tangential velocity at $\bar{z} = l$. The corresponding $\bar{u}_\theta(\bar{r}, l)$ displays a hyperbolic relation with the radial distance, thus causing $\bar{u}_\theta$ to approach a nonzero value at the sidewall and infinity at the centerline. In our effort at matching this free-vortex motion, both $\bar{C}$ and $\bar{D}$ are carefully selected. The resulting solution in Fig. 5b displays incremental shifts in the tangential velocity at different axial positions. Such behavior is identical to the one reported by Majdalani.[16]

C. Radial Velocity

The radial velocity in all of the models considered vanishes at the centerline due to axial symmetry. Furthermore, unlike simulated solid or hybrid rocket chambers, the vortex-fired rocket engines do not exhibit any radial velocity along the sidewall. In constructing our solution, the radial velocity profile does not appear explicitly in the inflow/outflow integrals of Eq. (39) and, as such, is not specifically imposed at the sidewall. Nonetheless, our results show that the radial velocity predicted by the series approximation along the inlet is strikingly similar to the profile that it seeks to mimic. This outcome may be attributed to $\bar{u}_z$ and $\bar{u}_r$ being intimately linked through the axisymmetric continuity relation, and this connection remains independent of the tangential velocity. So by imposing $\bar{u}_z$ at the boundary, we are implicitly securing its unique companion $\bar{u}_r$ at the same location. Regarding size considerations, the magnitude of $\bar{u}_r$ appears to be small in comparison to the axial and tangential speeds. It peaks as we approach the headwall as shown in Fig. 6 where a larger radial velocity is needed to assist the fluid in crossing from the outer vortex into the central core region.

IV. Conclusions

This study presents an exact Euler solution for the swirling bidirectional motion confined in a vortex chamber. What distinguishes this new set of analytical results stands in the model's capability to absorb arbitrary flow

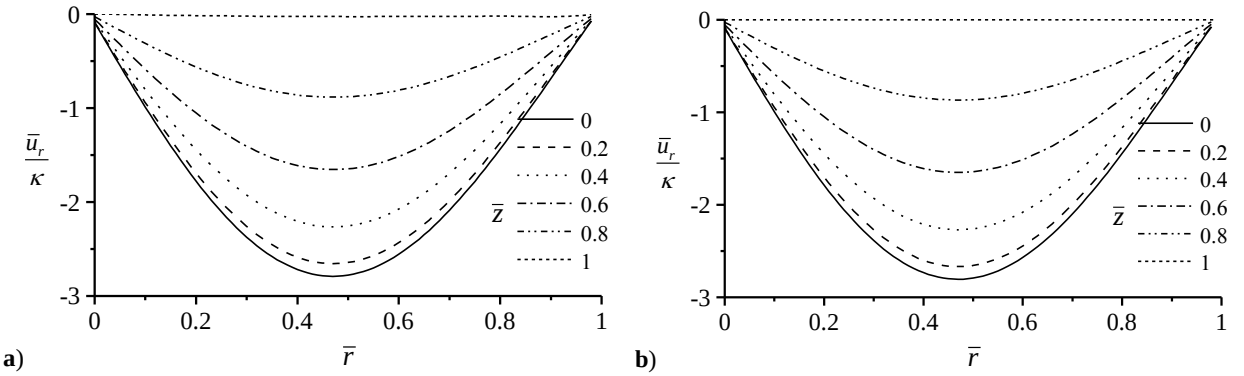

Figure 6. Radial variation of the radial velocity corresponding to a) Eq. (39) and b) both Beltramian and Trkalian models using $\upsilon = \pi/(2L)$.

conditions at the endwall boundaries. By changing the inlet/outlet conditions, the present formulation enables us to reproduce former analytical solutions based on the Brag- Hawthorne equation.

As it may be anticipated, our axial velocity displays the tendency to reproduce the same profiles imposed at the endwalls although its shapes may often shift in the axial direction as the flow changes from its basic configuration to the one prescribed at its boundary.

Concerning the swirl velocity, two keystone parameters, the swirl momentum constant $\bar{C}$ and the tangential surface parameter $\bar{D}$, are calibrated to match the tangential velocity at the boundary. We find that the choice of $\bar{C}$, and therefore $\bar{u}_\theta$ at the endwall, can affect the variation of the axial velocities throughout the domain.

For the radial velocity, it was shown that by strictly imposing the axial velocity at the inlet, we are indirectly setting the radial velocity as well due to these quantities being strongly connected through the continuity equation to the extent that specifying one is tantamount to specifying the other. In general, the magnitude of the radial velocity remains small compared to other flow components, except near the headwall where the radial velocity peaks and both the axial and tangential velocities reach their minima.

Acknowledgments

This material is based on work supported partly by the National Science Foundation and partly by the University of Tennessee Space Institute, through institutional cost sharing.

References

[1]Gloyer, P. W., Knuth, W. H., and Goodman, J., "Overview of Initial Research into the Effects of Strong Vortex Flow on Hybrid Rocket Combustion and Performance," CSTAR Fifth Annual Symposium Paper N96-16953, January 1993.

[2]Knuth, W. H., Bemowski, P. A., Gramer, D. J., Majdalani, J., and Rothbauer, W. J., "Gas-Fed, Vortex Injection Hybrid Rocket Engine," NASA Marshall Space Flight Center, SBIR Phase I Final Technical Rept. NASA/MSFC Contract NAS8-40679, Huntsville, AL, August 1996.

[3]Chiaverini, M. J., Malecki, M. J., Sauer, J. A., Knuth, W. H., and Majdalani, J., "Vortex Thrust Chamber Testing and Analysis for O2-H2 Propulsion Applications," AIAA Paper 2003-4473, July 2003.

[4]Matveev, I., Matveeva, S., and Serbin, S., "Design and Preliminary Test Results of the Plasma Assisted Tornado Combustor," AIAA Paper 2007-5628, July 2007.

[5]Vyas, A. B., Majdalani, J., and Chiaverini, M. J., "The Bidirectional Vortex. Part 1: An Exact Inviscid Solution," AIAA Paper 2003-5052, July 2003.

[6]Vyas, A. B., Majdalani, J., and Chiaverini, M. J., "The Bidirectional Vortex. Part 2: Viscous Core Corrections," AIAA Paper 2003-5053, July 2003.

[7]Vyas, A. B., Majdalani, J., and Chiaverini, M. J., "The Bidirectional Vortex. Part 3: Multiple Solutions," AIAA Paper 2003-5054, July 2003.

[8]Majdalani, J., and Vyas, A. B., "Rotational Axisymmetric Mean Flow for the Vortex Injection Hybrid Rocket Engine," AIAA Paper 2004-3475, July 2004.

[9]Majdalani, J., "Vortex Injection Hybrid Rockets," *Fundamentals of Hybrid Rocket Combustion and Propulsion*, edited by K. Kuo and M. J. Chiaverini, AIAA Progress in Astronautics and Aeronautics, Washington, DC, 2007, pp. 247-276.

[10]Vyas, A. B., and Majdalani, J., "Characterization of the Tangential Boundary Layers in the Bidirectional Vortex Thrust Chamber," AIAA Paper 2006-4888, July 2006.

[11]Batterson, J. W., and Majdalani, J., "On the Boundary Layers of the Bidirectional Vortex," AIAA Paper 2007-4123 June 2007.

[12]Batterson, J. W., and Majdalani, J., "Sidewall Boundary Layers of the Bidirectional Vortex," *Journal of Propulsion and Power*, Vol. 26, No. 1, 2010, pp. 102-112. doi: 10.2514/1.40442

[13]Majdalani, J., and Chiaverini, M. J., "On Steady Rotational Cyclonic Flows: The Viscous Bidirectional Vortex," *Physics of Fluids*, Vol. 21, No. 10, 2009, pp. 10360301-15. doi: 10.1063/1.3247186

[14]Maicke, B. A., and Majdalani, J., "A Constant Shear Stress Core Flow Model of the Bidirectional Vortex," *Proceedings of the Royal Society of London, Series A*, Vol. 465, No. 2103, 2009, pp. 915-935. doi: 10.1098/rspa.2008.0342

[15]Zhao, J. Q., and Abrahamson, J., "The Flow in Cylindrical Cyclones," *Developments in Chemical Engineering and Mineral Processing*, Vol. 11, No. 3-4, 2003, pp. 201-222. doi: 10.1002/apj.5500110403

[16]Majdalani, J., "Exact Eulerian Solutions of the Cylindrical Bidirectional Vortex," AIAA Paper 2009-5307, August 2009.
[17]Vyas, A. B., and Majdalani, J., "Exact Solution of the Bidirectional Vortex," *AIAA Journal,* Vol. 44, No. 10, 2006, pp. 2208-2216. doi: 10.2514/1.14872